Kinetic Monte Carlo simulations and cross-sectional scanning tunneling microscopy as tools to investigate the heteroepitaxial capping of self-assembled quantum dots

J. G. Keizer* and P. M. Koenraad

Department of Applied Physics, Eindhoven University of Technology, P.O. Box 513, 5600 MB, Eindhoven, The Netherlands

P. Smereka

Department of Mathematics, University of Michigan, Ann Arbor, Michigan 48109, United States

J. M. Ulloa, A. Guzman, and A. Hierro

Institute for Systems based on Optoelectronics and Microtechnology (ISOM), Universidad Politecnica de Madrid, Ciudad Universitaria s/n, 28040 Madrid, Spain

(Received 30 January 2012; revised manuscript received 13 April 2012; published 27 April 2012)

The growth of self-assembled quantum dots has been intensively studied in the last decade. Despite substantial efforts, a number of details of the growth process remain unknown. The reason is the inability of current characterization techniques to image the growth process in real time. In this work, this limitation is alleviated by the use of kinetic Monte Carlo simulations in conjunction with cross-sectional scanning tunneling microscopy. The two techniques are used to study the method of strain engineering as a procedure to control the height of quantum dots. We show that fully three-dimensional kinetic Monte Carlo simulations can be matched with the experimentally obtained morphology of buried quantum dots and that combination of the two techniques provides details of the growth process that hitherto could not be obtained.

DOI: 10.1103/PhysRevB.85.155326 PACS number(s): 61.46.−w

I. INTRODUCTION

In the last decade, an ever increasing understanding of heteroepitaxial growth has paved the way for the fabrication of a multitude of self-assembled nanostructures. Nowadays, nanostructures such as quantum rings,[1] quantum wires,[2] quantum dashes,[3] quantum rods,[4] and quantum dots (QDs)[5] can be grown with relative ease. Among these, QDs have, due to their 0-dimensional nature, received the most attention and are applied or suggested in QD lasers,[6,7] single-photon emitters,[8] single-electron transistors,[9] and spin manipulation.[10,11] As the electronic properties of QDs strongly depend on their size, shape, and chemical composition, a detailed knowledge of the growth process and the resulting QD morphology is needed in order to understand the involved physics and tune their properties. A large variety of imaging techniques are available to study the morphology, the dimensions, and the chemical composition of self-assembled QDs, e.g., scanning/transmission electron microscopy,[12] x-ray diffraction,[13] atomic force microscopy,[14,15] atom probe tomography,[16,17] and cross-sectional scanning tunneling microscopy (X-STM).[18] However, all the existing imaging techniques can only provide snapshots of the QDs *after* the growth is completed. At the moment, only a few techniques, e.g., reflection high-energy electron diffraction (RHEED),[19] *in situ* accumulated stress measurements,[20] and spectroscopic ellipsometry,[21] can give real-time information *during* the growth and thereby help monitoring the growth. But, if such techniques provide valuable information about the growth surface, the averaging nature of the techniques makes them of little use when studying atomic-scale processes such as intermixing or segregation. In this respect, kinetic Monte Carlo (KMC) simulations of the heteroepitaxial growth process can be of great value and provide further insight on the growth dynamics. However, such KMC simulations are computationally challenging[22,23] and still need validation by an experimental imaging technique.

In this paper, we present KMC results using recent developments in computational methods.[24] The KMC simulations are compared to atomically precise QD morphologies extracted from experimental X-STM images. These two techniques are used in conjunction to study strain engineering of the capping layer[25,26] as a method to control the height of quantum dots, an important parameter determining the QDs emission wavelength. We show that KMC simulations not only are in good agreement with the X-STM study, but also provide valuable details of the growth process that hitherto could not be obtained.

II. MATERIAL SYSTEM

The material system consists of four InAs/GaAs QD layers grown by molecular beam epitaxy on an *n*-doped GaAs [001]-oriented substrate. The growth process is initiated by the deposition of a 350-nm GaAs buffer layer at a temperature of 580 °C. The growth sequence of the first QD layer starts by the deposition of 2.7 monolayers (ML) of InAs at 450 °C and a growth rate of 0.04 ML s^{-1}. Next, the QD layer is overgrown with a 5-nm-thick $In_xGa_{1-x}As$ layer with $x = 0.00$, $x = 0.05$, $x = 0.10$, $x = 0.15$ for the four consecutive QD layers, respectively. This was done at 450 °C and at a growth rate of 0.75 ML s^{-1}. The indium content x was calibrated by comparing the RHEED oscillations of GaAs and InGaAs/GaAs quantum wells grown under the same conditions as the capping layers of the studied samples. Since the growth rate can be measured in this way with great accuracy, the uncertainty in the nominal indium contents should be very small. The QD layers will be numbered in the sequence as they were grown. On top of the capped QD layer, a 50-nm GaAs spacer layer is grown after which the growth sequence

 ©2012 American Physical Society

for the next QD layer begins. The total structure was capped with 200 nm of GaAs. Finally, an uncapped QD layer was grown on top.

III. METHODS

The X-STM measurements were performed at 77 K under UHV conditions ($p < 5 \times 10^{-11}$ mbar) on *in situ* cleaved (110) surfaces. Low-temperature ensures long-term stable tunnel conditions and facilitates imaging long stretches of sample without drift. The X-STM measurements were all done at high negative bias voltages and low tunnel currents ($V \approx -3$ V, $I \approx 20$ pA). At such tunnel conditions and with the color scale used, InAs (GaAs) rich regions appear bright (dark) in the topographic X-STM maps.

The surface of the strained material system relaxes outward upon cleavage. This minute outward displacement of the surface can be recorded in careful X-STM measurements. In conjunction with finite element (FE) calculations, this information can be used to deduce the local composition profile of the material system.[27,28] In this paper, the outward strain relaxation of the capping layers is modeled by two-dimensional FE calculations performed using the MEMS module of COMSOL Multiphysics.

Our KMC model for heteroepitaxial growth is based on the work of Orr *et al.*[29] and Lam *et al.*[22] This model was recently extended to allow for intermixing.[30,31] Briefly, the model is a solid-on-solid bond counting model in which elastic interactions are included using a ball and spring model and where only the surface atoms are mobile. The assumption that only surface atoms are mobile is a common restriction of many continuum and KMC models of epitaxial growth and stems from observations and calculations that mobility of surface atoms is far greater than atoms in the bulk (e.g., Mullins *et al.*[32]). The issue of bulk diffusion is somewhat controversial (e.g., Ratto *et al.*[33]), and while it is easy to include such effects in our KMC model, it is difficult to justify the mechanisms that would actually lead to bulk diffusion. For this reason, we have chosen to neglect it, however, as discussed in the following, this does not mean we ignore intermixing.

We shall treat GaAs and InAs as “atoms” and denote them as types 1 and 2, respectively. These atoms are assumed to be arranged on a simple cubic lattice. Since the model is a solid-on-solid model, each surface atom has material below it which can be composed of either type-1 or type-2 atoms. Although only surface atoms are allowed to move, this model can give rise to subsurface intermixing. This happens because there is no restriction on the type of atom below the surface, and the combination of adatom hopping and thermal roughening of the surface allows atoms initially on the surface to be incorporated into the material below. This issue is discussed in more detail in Ref. 34. Along these same lines, Haxha *et al.*[35] reported that intermixing of three atomic layers was needed to achieve good agreement with experimental results. This is not in contradiction with the results we present below since the model presented by Haxha *et al.* is a mean-field model, and in order to describe the intermixing captured by our KMC model, it was necessary to explicitly include exchange between surface and subsurface atoms.

The KMC will now be described in more detail. The hopping rate of the pth surface atom is given by

$$R_p = R_0 \exp\left[\frac{-E_D - B + \Delta W}{kT}\right],$$

where kT is the thermal energy, $R_0 = 10^{12}\ \mathrm{s}^{-1}$ the diffusion constant, E_D the energy barrier for diffusion of an InAs adatom on GaAs, ΔW the change in elastic energy when removing an atom, and B the total bond energy of an atom given by

$$B = B_{11} + B_{22} + B_{12} - (a + 4b + 4c)\gamma_{12},$$

where the last term is added to make $B = 0$ for an InAs adatom on GaAs, and with

$$B_{\alpha\beta} = \left(aN_{\alpha\beta}^{(n)} + bN_{\alpha\beta}^{(nn)} + cN_{\alpha\beta}^{(nnn)}\right)\gamma_{\alpha\beta}.$$

As well, $N_{\alpha,\beta}^{(n)}$ denotes the total number of bonds of type $\alpha - \beta$ connecting the surface atom and its nearest neighbors, $N_{\alpha\beta}^{(nn)}$ and $N_{\alpha\beta}^{(nnn)}$ are analogously defined but for next-nearest neighbors and next-to-next-nearest neighbors, respectively. The strength of the interaction is $\gamma_{\alpha\beta}$ and the form of the anisotropy can be controlled with the choices of a, b, and c. In our simulations we take $a = 0.3$, $b = 0.5$, and $c = 1.0$. These values were chosen so that the (100) surface has a slightly lower surface energy than the (111) and (110) surfaces, thereby giving rise to pyramidally shaped quantum dots. In addition, we take $\gamma_{11} = 0.2506$, $\gamma_{12} = 0.2217$, $\gamma_{22} = 0.2169$, and $E_D = 0.8792$ all in eV.

While $B + E_D$ represents the contribution to the energy barrier from local interactions, ΔW is the contribution from elastic interactions. As mentioned, this is taken to be the change in the total elastic energy that occurs when removing the pth surface atom. This choice guarantees that the rates will satisfy detailed balance.[22] The elastic interactions are accounted for by using a ball and spring model with longitudinal and diagonal springs having spring constants k_L and k_D, respectively. The elastic effects arise because the natural bond lengths of GaAs and InAs are different. We will, respectively, denote these lengths as ℓ_1 and ℓ_2, the misfit is then $\mu = (\ell_2 - \ell_1)/\ell_1$. In our simulations, we take $k_L = 2.89\ \mathrm{eV}/\ell_1^2$, $k_D = 9.64\ \mathrm{eV}/\ell_1^2$, and $\mu = 0.075$.

Many of the parameter values for the KMC simulations were chosen to roughly approximate the physical properties of GaAs. More specifically, the value $\gamma_{11} = 0.2506$ eV gives the surface energy of a (110) facet of a simple cubic lattice of approximately 852 erg cm^{-2}, which is a reasonable value for the surface energy of GaAs.[36] The values γ_{22} and γ_{12} were chosen so that material 2 would easily wet material 1, resulting in a wetting layer of approximately 1.5 ML. The spring constants were picked to approximate the bulk elastic properties of GaAs. These values yield the following elastic coefficients, $C_{11} \approx 7.9 \times 10^{11}$ dyne cm^{-2} and $C_{12} \approx 3.4 \times 10^{11}$ dyne cm^{-2}, which are reasonable values for GaAs. The quantity E_D, the energy barrier of diffusion of atoms of type 2 on a substrate of type 1, was more difficult to estimate since it does not correspond directly to a physical event, but instead represents an effective barrier for the diffusion of an InAs “atom” on a surface of GaAs. Since this seems too difficult to estimate, E_D was adjusted to get reasonable results. If E_D is chosen too large, the result is too little diffusion and

three-dimensional (3D) islands would not form, whereas if it is chosen too small the islands would erode too much upon capping. Nevertheless, the current choice seems reasonable.

The computation of ΔW is nonlocal and can be quite expensive to evaluate. However, it was shown that for a vast number of moves, the elastic displacement field can be updated locally, and only when this fails a global update is needed.[37] The global update itself is determined in an efficient manner using a multigrid method coupled with an artificial boundary condition to account for the semi-infinite substrate.[23,38] For this paper, an even faster approach was used.[24] Here, loosely speaking, the elastic field is not updated when atoms with a low coordination number move. This approximation has been carefully verified and the result is a code that is 15 times faster than that reported in Ref. 31.

IV. RESULTS

We start the X-STM analysis of the QD layers by investigating the morphology of the InGaAs layer in-between the QDs. In Fig. 1, X-STM current maps of representative stretches of the InGaAs layer as found in all four QD layers are shown. The indium fraction in the $In_xGa_{1-x}As$ capping layer was nominally increased from $x = 0.00$ to 0.15 in the consecutive QD layers. First, we consider the QD layer where the capping layer consists of a pure GaAs layer. During the initial stage of capping, strain induced by the lattice mismatch between InAs and GaAs drives mass transport of QD material (in this case indium) to regions in-between the QDs.[39,40] Upon further capping, this indium and the indium that was already present in the wetting layer segregate toward the growth front, resulting in an exponential decaying indium composition profile along the growth direction.[28] A quick glance at the X-STM image of Fig. 1(a) shows that this indeed seems to be the case for the first QD layer. The other three QD layers were overgrown with an $In_xGa_{1-x}As$ layer ($x > 0$). In these layers, the indium composition profile should therefore resemble that of a top hat with an additional exponential decaying indium composition profile due to segregation of the wetting layer. For capping layers with an indium fraction of $x = 0.05$ and 0.10, the final InGaAs layer between the QDs is nicely defined [see Figs. 1(b) and 1(c)]. However, looking at Fig. 1(d), this is evidently different for the fourth capping layer, which has the highest indium fraction ($x = 0.15$) of all layers. In contrast to the quasi-quantum wells found in the second and third layers that have a uniform thickness of 6.3 nm, here, the thickness is found to vary in the range 4.0–7.5 nm. We will now analyze the first three layers in more detail.

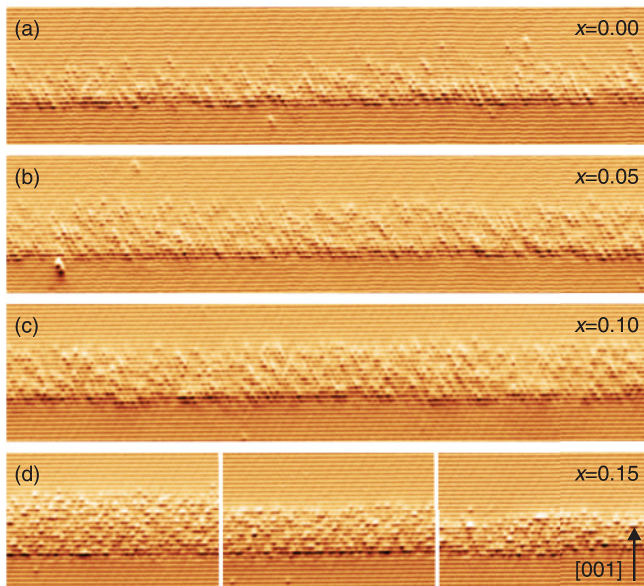

FIG. 1. (Color online) 85 × 18 nm^2 mean filtered X-STM current map of the four consecutive QD layers. Individual indium atoms can be distinguished. The indium fraction x of the capping layer is increased in the consecutive layers. (a) Wetting layer + GaAs capping; (b)–(d) wetting layer + InGaAs capping. Strong variations in the thickness of the final InGaAs layer at different parts of the layer are observed in (d).

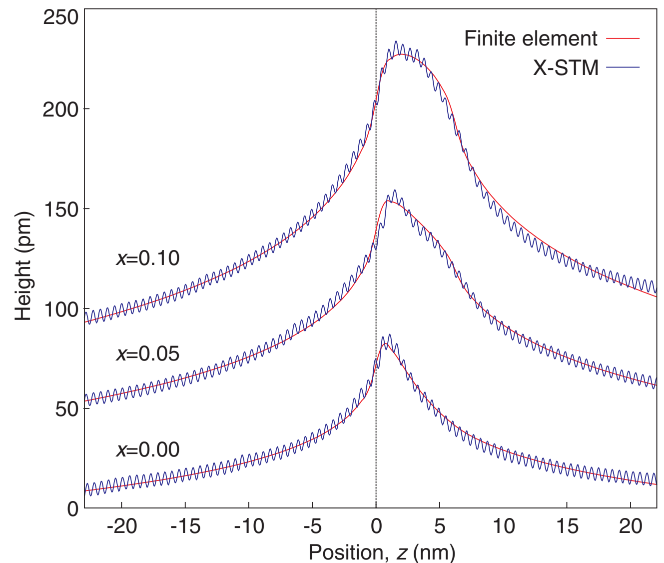

FIG. 2. (Color online) Outward relaxation profiles of the InGaAs layers in-between the QDs as measured by X-STM (blue) and the results of the FE calculations (red) for the first three QD layers. The oscillations in the X-STM profile represent the atomic corrugation.

To make the analysis more quantitative, we deduce the indium composition profile of each InGaAs layer between the QDs from the surface relaxation. This outward relaxation is the result of strain induced by the lattice mismatch between InAs and GaAs and is simulated by means of finite element (FE) calculations. For the first layer, the function $a\exp(-z/b)$, representing the segregation of indium from the wetting layer,[28] was used as an input for the FE modeling. In this equation, $z = 0$ nm corresponds with the start of the wetting layer and positive z values represent the growth direction. By adjusting the initial indium fraction a and the inverse decay constant b until the calculated outward relaxation matches the outward relaxation as measured by X-STM (see Fig. 2), the indium composition profile of the wetting layer can be determined. The values that were found to yield the best match are $a = 0.236 \pm 0.002$ and $b = 1.48 \pm 0.02$ nm. Next, we extend such analysis to the second and third layers. In these layers, multiple indium sources contribute to the total amount of indium present in the final InGaAs layer in-between the

QDs. First, a wetting layer is present prior to capping. Second, mass transport of indium from the QDs to the InGaAs layer occurs during the initial stages of capping. Third, additional indium is deposited during capping. To account for this, we added an exponential decaying indium composition profile, similar to the one found for the case of capping with pure GaAs to a top-hat indium composition profile. The function describing the indium fraction is now given by $a\exp(-z/b) + x$. The values of x are taken from the nominal indium contents ($x = 0.05$, $x = 0.10$). Since the parameter b is determined by the temperature and the chemical properties of the individual indium atoms, we assume it to be the same as in the case of capping with pure GaAs. This only leaves a for fitting, which is a measure for the amount of indium transferred from the QD to the InGaAs capping layer and the indium already present in the wetting layer. We found a match between the calculated and the experimentally observed outward relaxation for $a = 0.165 \pm 0.002$; $a = 0.105 \pm 0.002$ nm for the second and third capping layers, respectively. The fact that the value of a decreases with increasing x can be explained by better lattice matching between the capping layer and the QD with an increasing indium fraction in the capping layer. As a result, the QD will be less strained. Since, strain is the major driving force for mass transport of indium from the QD to the wetting layer during capping, a reduced strain mismatch will result in a lower indium content in the final InGaAs layer in-between the QDs. The comparison between the outward relaxation profiles from the X-STM measurements and the results of the FE calculations are shown in Fig. 2.

We now extend the analysis to the QDs themselves. From atomic force microscopy (AFM) measurements, the height of the uncapped QDs was determined to be 5.6 nm with a standard deviation of $\sigma = 0.7$ nm. A total of 113 QDs in approximately 10 μm of QD layer were imaged by X-STM. Just as in the case of the InGaAs layers, we will treat the first three QD layers first, leaving the fourth layer for later. In Fig. 3, topographic X-STM maps of representative QDs as found in the first three QD layers are shown. The average height of the QDs as determined by X-STM is found to be 3.9, 4.6, and 5.1 nm ($\sigma = 0.4$ nm) for capping layers with an indium fraction of $x = 0.00$, 0.05, and 0.10, respectively. Within the standard deviations, this is a linearly increasing trend. As previously discussed, this result can be explained by the strain reduction with increasing indium fraction in the capping layer. As the strain mismatch is reduced in the consecutive QD layers, the driving force for mass transport from QD material into the capping layer is also reduced. We already explained the observed composition profile of the InGaAs layer in-between the QDs by this mechanism. Given the height of the uncapped QDs as determined from the AFM measurements, decomposition of the QDs is almost completely suppressed for a capping layer with an indium fraction of $x = 0.10$. Surprisingly, the linear trend of increasing QD height as function of indium fraction in the capping layer is found to break down in the current material system when the indium fraction reaches $x = 0.15$, i.e., in the fourth QD layer. In this layer, the QD height is found to be 3.7 nm, which is smaller than the QD height in the first layer.

The decrease of the QD height and the variation in the thickness of the InGaAs layer in-between the QDs [see

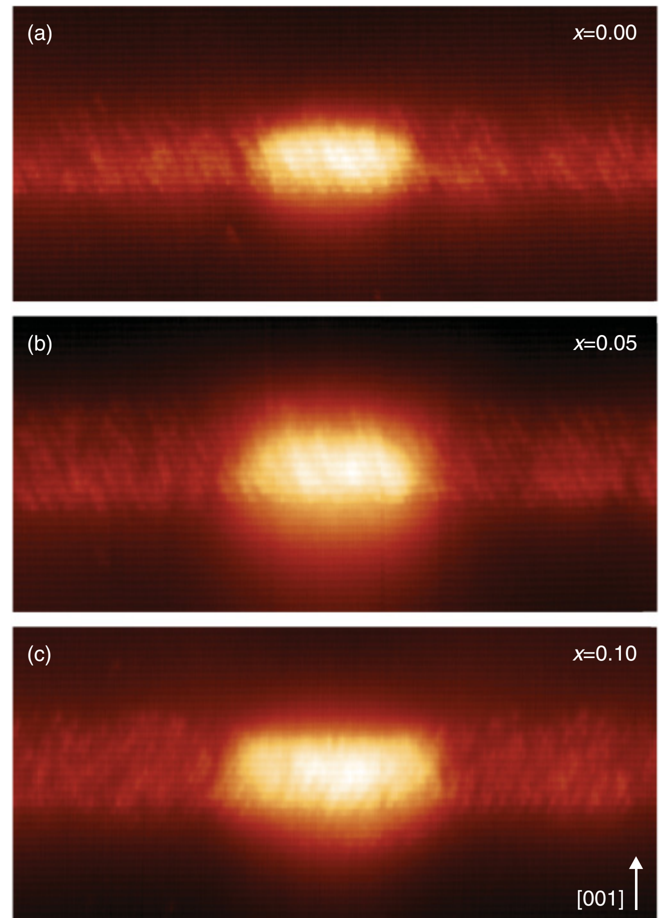

FIG. 3. (Color online) 50×22 nm^2 topographic X-STM maps of representative QDs as found in the first three QD layers. The indium fraction in the capping layer x was increased in the consecutive QD layers.

Fig. 1(d)] are an indication that an additional mechanism is involved during the overgrowth of the fourth QD layer. This can indeed be seen in Fig. 4, which shows a 880-nm-long uninterrupted stretch of the fourth QD layer. A couple of striking features are visible. First, as we mentioned above, the thickness of the InGaAs layer varies: long, relatively thick, and uniform stretches are interrupted with variations in thickness and homogeneity close to the QDs. Second, indium-depleted regions are observed directly next to the QDs. Third, some of the QDs are asymmetrically shaped. Fourth, the QDs have a smaller height than in the first three QD layers. Since the observed peculiarities might result from several processes occurring at different stages of overgrowth, it is difficult to explain them solely from the X-STM measurements.

We have used KMC simulations to further analyze the growth processes. Here, it needs to be stressed that the purpose of the KMC simulations is to indicate trends in the growth processes only. In Fig. 5, a bird's eye view of the uncapped QDs grown in the KMC simulation is shown. These uncapped QDs are subsequently overgrown with 10-ML-thick $In_xGa_{1-x}As$ layers of which the indium fraction x was consecutively increased. Finally, the GaAs spacer layer is deposited on top of the InGaAs capping. The results are summarized in Fig. 6, which shows two-dimensional cross sections (analog

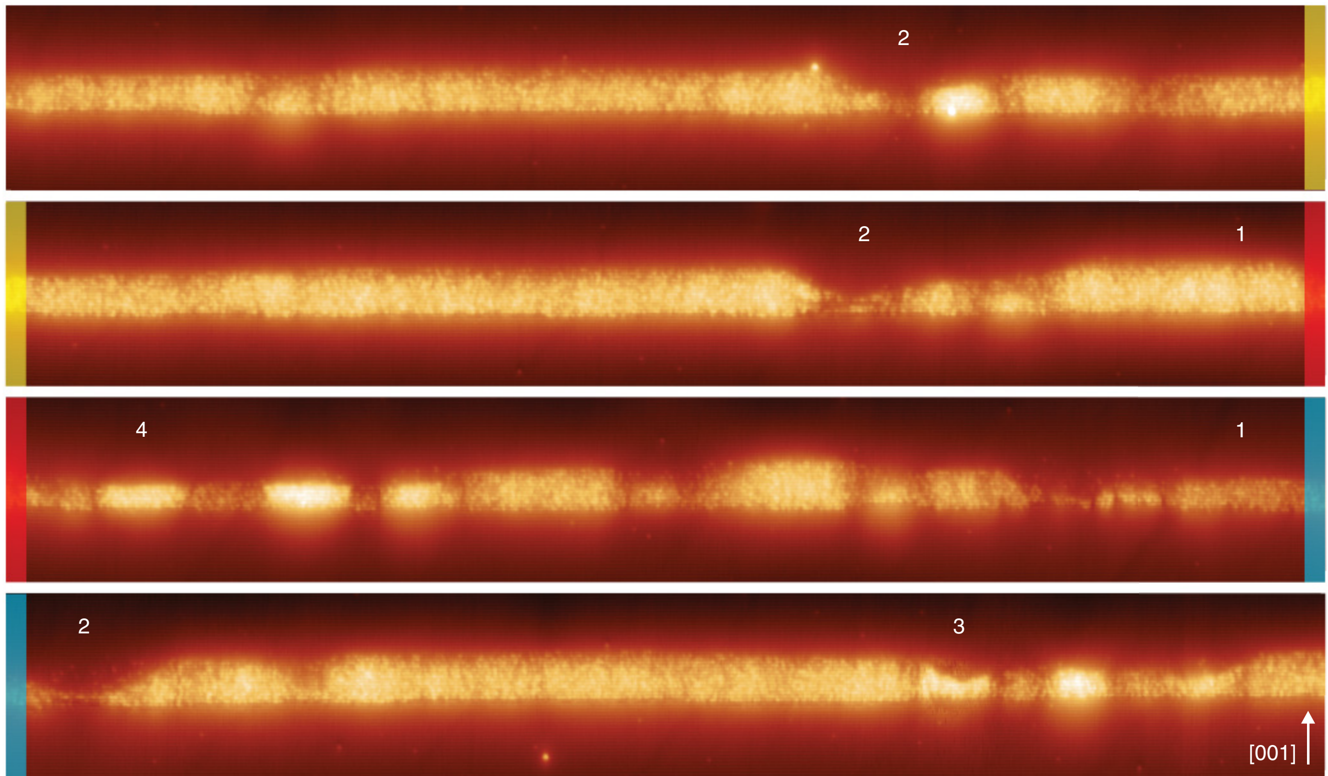

FIG. 4. (Color online) 880×30 nm^2 topographic X-STM map of the fourth QD layer. The QDs were capped with an $In_{0.15}Ga_{0.85}As$ layer. The colored semitransparent regions at the sides mark the overlay of consecutive images. Examples of the four observed peculiarities are marked: (1) varying thickness of the InGaAs layer in-between the QDs, (2) indium-depleted regions, (3) asymmetrically shaped QDs, and (4) reduced QD height.

to the (110) cleavage plane exposed in X-STM) through the fully three-dimensional KMC data sets. Each rectangle in the figure represents an "atom" and has the height and width of one lattice constant. The cross sections through the uncapped QDs [see Fig. 6(a)] show that the QDs have a height of 10 rectangles (=6.0 nm) and are connected by a submonolayer of

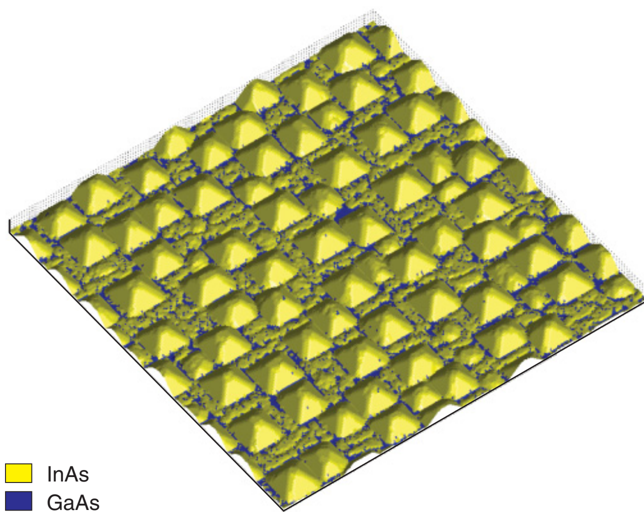

FIG. 5. (Color online) Bird's eye view of the uncapped QDs grown in the KMC simulations. The computational grid consists of 250×250 "atoms."

indium. Upon capping of the QDs with a pure GaAs layer [see Fig. 6(b)], indium is transported away from the QDs and forms a wetting layer with a decaying indium concentration along the growth direction. As a result of this mass transport, the height of the QDs in this layer is reduced to ≈3.6 nm. Note that the QD morphology agrees nicely with the experimentally observed QDs in the first layer. Since the growth front is flat and the QDs are already fully capped, subsequent growth of the GaAs spacer layer has no consequences on the QD morphology. If the indium fraction in the capping layer is set to $x = 0.05$ and 0.10 [see Figs. 6(c) and 6(d)], the KMC simulations show an increase, compared to a pure GaAs capping, of the QD height to ≈4.2 and ≈4.8 nm, respectively. Here, the reduction in strain between the QDs and the capping layer due to better lattice matching reduces the mass transport of indium originally located in the QDs. This trend of increasing QD height with increasing indium fraction in the capping layer is in good agreement with the X-STM measurements and previous results,[41] and again illustrates that strain engineering of the capping layer is an effective way of controlling the height of QDs.

If the indium fraction in the capping layer is further increased to $x = 0.15$ and 0.20, the system enters another regime [see Figs. 6(e) and 6(f)]. The height of the QDs is now increased to ≈5.4 and ≈6.0 nm, respectively, the latter corresponding to the height of the uncapped QDs. In these two QD layers, the atomic layers in the top of the QDs are not as pure in indium as the bottom part of the QDs. The border between the two regions [marked in Figs. 6(e)

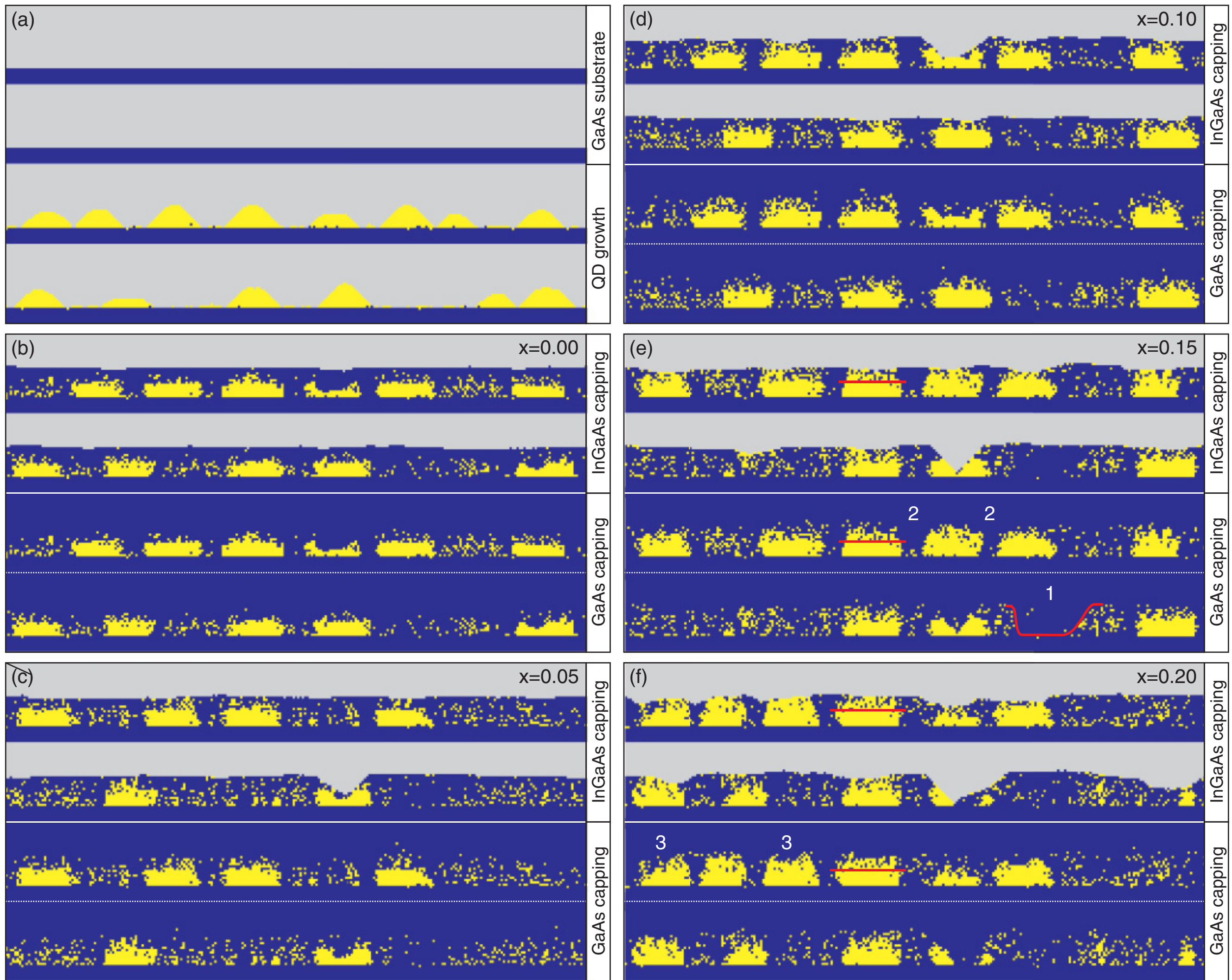

FIG. 6. (Color online) 140 × 20 nm^2 cross sections through the KMC data set. Each window shows two stretches and two situations. (a) GaAs substrate (top two panes) and the uncapped QDs (bottom two panes). These uncapped QDs represent the initial configuration for all performed KMC simulations of the capping process. (b)–(f) The indium fraction x is increased in the consecutive windows, which show the situation after the growth of the InGaAs capping layer (top two panes), and after the growth of the pure GaAs spacer layer (bottom two panes). (e), (f) The horizontal red line marks, for an exemplary QD, the boundary between the pure InAs region and the region of phase separation. Examples of the three observed peculiarities are marked: (1) variation in the thickness of the InGaAs layer between the QDs (solid red line), (2) indium-depleted regions, and (3) asymmetrically shaped QDs.

and 6(f) with a red horizontal line for an exemplary QD] is well defined, indicating that two independent processes that sequentially play out are involved. The first process is the already discussed mass transport of indium originally present in the QDs during the initial stage of capping. The second process, occurring at a later stage during capping, is the QD strain-driven phase separation of InGaAs into indium-rich and gallium-rich regions. The indium-rich regions preferentially form on top of the QDs where they minimize the total strain of the system. This process has been observed in InAs/GaAs QDs that were capped with an InGaAs layer,[42] and was used to achieve columnar InGaAs/GaAs QDs.[4] The KMC simulations show that the phase separation gets stronger with increasing indium fraction in the capping layer [see, e.g., Figs. 6(d) and 6(f)]. Both X-STM measurements and KMC simulations reveal that the involved indium atoms come from areas directly around the QDs. As a consequence, these regions are being depleted with indium when the phase separation on top of the QDs kicks in.

Three out of the four peculiarities observed by X-STM in the fourth layer are also present in the KMC simulations where the indium fraction in the capping layer is the highest: (1) large variations in the thickness of the InGaAs layer in-between the QDs, (2) indium poor/free regions immediately next to the QDs, and (3) asymmetrically shaped QDs. Exemplary cases of these peculiarities are marked in Figs. 6(e) and 6(f). In contrast to X-STM, the KMC simulations allow the investigation of the intermediate stages of the growth process. The results show that during the growth of the capping layers, the surface becomes unstable, leading to a considerable roughening. The onset of such surface instability and roughening of the surface is well documented for $In_xGa_{1-x}As$ quantum wells[43] as a

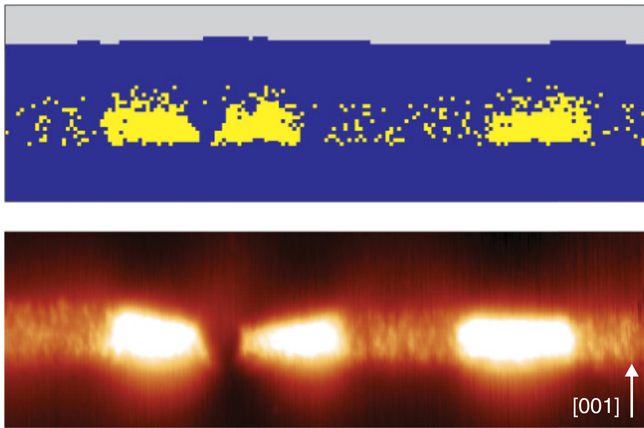

FIG. 7. (Color online) Comparison of two cross sections as obtained in the KMC simulations (top) and by X-STM measurements (bottom) for a high-indium-content capping layer.

function of the indium concentration and layer thickness. The critical thickness for quantum wells with $x = 0.15$ is $\approx$20 nm. This is well beyond the 5-nm-thick capping layer for which we observed the instabilities. We argue that the presence of the InAs QDs locally introduces additional strain in the system, which lowers the critical thickness considerably. Furthermore, the fourth QD layer in the sample is subjected to the strain field of the first three QD layers, which might further lower the critical thickness. However, we think this contribution is of lesser importance since the observed surface instabilities are manifested most prominently near the QDs in the fourth layer. At these sites, the thickness of the capping layer is significantly reduced and, as a result, some of the QDs are not fully capped. The exposed top of these QDs partially erodes upon further capping, giving rise to the asymmetrically shaped QDs. Although this process leads to a higher degree of QD erosion, it can not reproduce the strong reduction in QD height observed in the X-STM measurements. The phase separation on top of the QDs and the roughening of the surface, both processes that are driven by QD strain, are together responsible for the variation in the thickness of the InGaAs in-between the QDs.

The mentioned surface instability that appears at high In contents is a main factor determining the growth process, and can give rise to peculiar QD structures such as those shown in Fig. 7. In this figure, a cross section from the KMC simulations is compared with the X-STM results. Although the matching QD positions are completely coincidental, the agreement between the morphology of the QD layer in the KMC simulation and the actual QD layer is striking. This, and the results presented above, demonstrate the potential of KMC simulation as an excellent tool to investigate the epitaxial growth of nanostructures.

V. CONCLUSION

The combination of X-STM and KMC simulations was used to investigated the capping of InAs/GaAs QDs with a strained InGaAs layer. FE simulations of the surface relaxation show that mass transport from the QD to the capping layer is reduced with increasing indium content in the capping layer and leads to an increase of the QD height. This result is reproduced in the KMC simulations. The KMC simulations showed that a 5-nm-thick capping layer becomes unstable above a critical indium fraction, resulting in peculiar features in the QD layer: variations in the thickness of the InGaAs layer in-between the QDs, indium-depleted regions immediately next to the QDs, and asymmetrically shaped QDs. The KMC simulations show that these features can be explained in terms of mass transport from the QD to the capping layer, phase separation on top of the QD, and roughening of the surface. The only feature that could not be reproduced in the KMC simulation is the reduction of the QD height in the layer with the highest indium content. To summarize, it was shown that strain engineering of the capping layer can be used to control the QD height. We have shown that KMC simulations, in combination with X-STM, are a very valuable asset in understanding the dynamics of QD growth. Furthermore, we feel that the current results are an indication that KMC simulations might be able to predict the outcome of the growth process in the future.

ACKNOWLEDGMENTS

We thank STW-VICI under Grant No. 6631 for their financial support of the work done in Eindhoven. The work in Ann Arbor has been supported by NSF through Grants No. DMS-0810113, No. DMS-0854870, and No. DMS-1115252. The Work in Madrid has been supported by Comunidad de Madrid through Projects No. P2009/ESP-1503 and No. CCG10-UPM/TIC-4932.

*j.g.keizer@tue.nl

[1] C. Somaschini, S. Bietti, N. Koguchi, and S. Sanguinetti, Nano Lett. **9**, 3419 (2009).

[2] J. G. Keizer, M. Jo, T. Mano, T. Noda, K. Sakodam, and P. M. Koenraad, Appl. Phys. Lett. **98**, 193112 (2011).

[3] M. Jo, T. Mano, and K. Sakoda, Appl. Phys. Express **3**, 045502 (2010).

[4] J. He, R. Notzel, P. Offermans, P. M. Koenraad, Q. Gong, G. J. Hamhuis, T. J. Eijkemans, and J. H. Wolter, Appl. Phys. Lett. **85**, 2771 (2004).

[5] R. Nötzel, Semicond. Sci. Technol. **11**, 1365 (1996).

[6] S. Fafard, K. Hinzer, S. Raymond, M. Dion, J. McCaffrey, Y. Feng, and S. Charbonneau, Science **274**, 1350 (1996).

[7] F. Heinrichsdorff, M.-H. Mao, N. Kirstaedter, A. Krost, D. Bimberg, A. O. Kosogov, and P. Werner, Appl. Phys. Lett. **71**, 22 (1997).

[8] Z. Yuan, B. E. Kardynal, R. M. Stevenson, A. J. Shields, C. J. Lobo, K. Cooper, N. S. Beattie, D. A. Ritchie, and M. Pepper, Science **295**, 102 (2002).

[9] K. Yano, T. Ishii, T. Hashimoto, T. Kobayashi, F. Murai, and K. Seki, IEEE Trans. Electron Devices **41**, 1628 (1994).

[10] D. Loss and D. P. DiVincenzo, Phys. Rev. A **57**, 120 (1998).

[11] S. Chakrabarti, M. A. Holub, P. Bhattacharya, T. D. Mishima, M. B. Santos, M. B. Johnson, and D. A. Blom, Nano Lett. **5**, 209 (2005).
[12] P. Wang, A. L. Bleloch, M. Falke, P. J. Goodhew, J. Ng, and M. Missous, Appl. Phys. Lett. **89**, 072111 (2006).
[13] J. Novák, V. Holý, J. Stangl, T. Fromherz, Z. Zhong, G. Chen, G. Bauer, and B. Struth, J. Appl. Phys. **98**, 073517 (2005).
[14] I. Tanaka, I. Kamiya, H. Sakaki, N. Qureshi, S. J. Allen, and P. M. Petroff, Appl. Phys. Lett. **74**, 844 (1999).
[15] M. da Silva, A. A. Quivy, P. P. Gonzalez-Borrero, E. Marega, and J. R. Leite, J. Cryst. Growth **241**, 19 (2002).
[16] M. Müller, A. Cerezo, G. D. W. Smith, L. Chang, and S. S. A. Gerstl, Appl. Phys. Lett. **92**, 233115 (2008).
[17] A. D. Giddings, J. G. Keizer, M. Hara, G. J. Hamhuis, H. Yuasa, H. Fukuzawa, and P. M. Koenraad, Phys. Rev. B **83**, 205308 (2011).
[18] J. K. Garleff, J. M. Ulloa, P. M. Koenraad, and B. Bhushan, *Scanning Probe Microscopy in Nanoscience and Nanotechnology 2*, edited by B. Bhushan (Springer, Berlin, 2011), p. 321.
[19] A. Feltrin and A. Freundlich, J. Cryst. Growth **301-302**, 38 (2007).
[20] D. Alonso-Álvarez, B. Alén, J. M. Ripalda, A. Rivera, A. G. Taboada, J. M. Llorens, Y. González, L. González, and F. Briones, e-print arXiv:1102.4944.
[21] M. King, X. Du, A. S. Cavanagh, and A. W. Weimer, Nanotechnology **19**, 445401 (2008).
[22] C.-H. Lam, C.-K. Lee, and L. Sander, Phys. Rev. Lett. **89**, 216102 (2002).
[23] G. Russo and P. Smereka, J. Comput. Phys. **214**, 809 (2006).
[24] T. P. Schulze and P. Smereka (unpublished).
[25] K. Nishi, H. Saito, S. Sugou, and J.-S. Lee, Appl. Phys. Lett. **74**, 1111 (1999).
[26] F. Guffarth, R. Heitz, A. Schliwa, O. Stier, N. N. Ledentsov, A. R. Kovsh, V. M. Ustinov, and D. Bimberg, Phys. Rev. B **64**, 085305 (2001).
[27] G. R. Liu and S. S. Q. Jerry, Semicond. Sci. Technol. **17**, 630 (2002).
[28] P. Offermans, P. M. Koenraad, R. Nötzel, J. H. Wolter, and K. Pierz, Appl. Phys. Lett. **87**, 111903 (2005).
[29] B. G. Orr, D. Kessler, C. W. Snyder, and L. Sander, Europhys. Lett. **19**, 33 (1992).
[30] A. Baskaran, J. Devita, and P. Smereka, Continuum Mech. Thermodyn. **22**, 1 (2009).
[31] T. P. Schulze and P. Smereka, Commun. Comput. Phys. **10**, 1089 (2011).
[32] W. W. Mullins, J. Appl. Phys. **28**, 333 (1957).
[33] F. Ratto, G. Costantini, A. Rastelli, O. Schmidt, K. Kern, and F. Rosei, J. Exper. Nanosci. **1**, 279 (2006).
[34] A. Baskaran and P. Smereka, J. Appl. Phys. **111**, 044321 (2012).
[35] V. Haxha, I. Drouzas, J. Ulloa, M. Bozkurt, P. Koenraad, D. Mowbray, H. Liu, M. Steer, M. Hopkinson, and M. Migliorato, Phys. Rev. B **80**, 165334 (2009).
[36] C. Messmer, J. Appl. Phys. **52**, 4623 (1981).
[37] T. P. Schulze and P. Smereka, Mech. Phys. Solids **57**, 521 (2009).
[38] G. Russo and P. Smereka, Multiscale Model. Simul. **5**, 130 (2006).
[39] G. Costantini, A. Rastelli, C. Manzano, P. Acosta-Diaz, R. Songmuang, G. Katsaros, O. Schmidt, and K. Kern, Phys. Rev. Lett. **96**, 226106 (2006).
[40] J. M. Ulloa, I. W. D. Drouzas, P. M. Koenraad, D. J. Mowbray, M. J. Steer, H. Y. Liu, and M. Hopkinson, Appl. Phys. Lett. **90**, 213105 (2007).
[41] J. M. Ulloa, C. Çelebi, P. M. Koenraad, A. Simon, E. Gapihan, A. Letoublon, N. Bertru, I. Drouzas, D. J. Mowbray, M. J. Steer, and M. Hopkinson, J. Appl. Phys. **101**, 081707 (2007).
[42] M. V. Maximov, A. F. Tsatsulnikov, B. V. Volovik, D. S. Sizov, Y. M. Shernyakov, I. N. Kaiander, A. E. Zhukov, A. R. Kovsh, S. S. Mikhrin, V. M. Ustinov, Z. I. Alferov, R. Heitz, V. A. Shchukin, N. N. Ledentsov, D. Bimberg, Y. G. Musikhin, and W. Neumann, Phys. Rev. B **62**, 16671 (2000).
[43] T. G. Andersson, Z. G. Chen, V. D. Kulakovskii, A. Uddin, and J. T. Vallin, Appl. Phys. Lett. **51**, 752 (1987).